Plane Parallel Albedo Biases from Satellite Observations. Part I: Dependence on Resolution and Other Factors

LAZAROS OREOPOULOS

Department of Atmospheric and Oceanic Sciences, McGill University, Montreal, Quebec, Canada

ROGER DAVIES

Institute of Atmospheric Physics, The University of Arizona, Tuscon, Arizona

(Manuscript received 8 August 1996, in final form 4 August 1997)

ABSTRACT

Due to cloud heterogeneity and the nonlinear dependence of albedo on cloud water content, the average albedo of a cloudy scene found by calculating the albedo of independent pixels within the scene tends to be different from the albedo calculated using the average cloud water in the scene. This difference, termed the plane parallel albedo bias (PPH bias), which has previously been estimated from limited case studies, is evaluated here for the first time using an extensive set of Advanced Very High Resolution Radiometer data over oceanic scenes. This dataset yields visible PPH biases that range from 0.02 to 0.30, depending in part on the size of the scene, the viewing–illumination directions, and the assumptions made retrieving cloud optical depths.

The PPH biases increase when atmospheric effects are accounted for but are relatively insensitive to assumptions about cloud microphysics. Due to the limitations of a one-dimensional retrieval, they tend to increase with solar zenith angle and to be larger in the backscattering than the forward scattering direction. Placed in the context of those general circulation models that do not provide subgrid-scale information on cloud amount, these biases are even larger. PPH biases in the broadband-reflected shortwave flux from general circulation models are estimated to exceed 30 W m^{-2}, typically requiring the introduction of a compensatory bias in the model's treatment of cloud water content.

The resolution of the satellite sensor and the averaging/sampling of the satellite substantially influences the calculated PPH bias. The authors find a significant drop in albedo bias (~0.02–0.05) when averaging/sampling original local area coverage (LAC) data to global area coverage (GAC) resolution or when Landsat data were averaged to LAC resolution. These results, along with stochastic simulations of internal LAC pixel variability indicate that the bias discrepancies among variable resolution satellite data are mostly due to the neglect of subpixel cloud fraction, which makes clouds appear thinner than they actually are.

1. Introduction

It is well known to GCM modelers that unmodified use of the mean cloud optical depth in a typical GCM grid cell tends to overestimate the albedo. Thus the conventional GCM assumption that clouds are horizontally homogeneous on scales of ~100 km forces the modification of cloud water amounts to unrealistically low values (Harshvardhan and Randall 1985; Cahalan et al. 1994a; Barker 1996) in order to match the observed top of the atmosphere (TOA) albedos.

The reason for this overestimate is found in the nonlinear dependence of albedo on optical depth, which is illustrated in Fig. 1a for the case of spherical albedo (i.e., albedo integrated over solar zenith angle), for the water droplet phase function used in International Satellite Cloud Climatology Project (ISCCP) retrievals. The convex nature of the albedo curve implies, for example, that for the simplest case of an optical depth distribution consisting of only two values, the average of the albedos corresponding to the two optical depths is smaller than the albedo corresponding to mean optical depth. This conclusion can be extended to any optical depth distribution and is demonstrated in Fig. 1a for distributions generated with Cahalan et al.'s (1994a) fractal ''bounded cascade'' model. These distributions have mean optical depth indicated by the abscissa and ratio of mean to standard deviation equal to 1.07. The two curves of the figure correspond to the plane parallel homogeneous (PPH) albedo, found from the mean optical depth of the distribution and the so-called independent pixel (IP) albedo found by averaging the albedos of individual cloudy pixels of the distribution. Inasmuch as these individual albedos are accurate, the IP albedo is a close representation of the average albedo of the scene from which the distribution is drawn, but

Corresponding author address: Dr. Roger Davies, Institute of Atmospheric Physics, The University of Arizona, P.O. Box 210081, Room 542, Tucson, AZ 85721-0081.

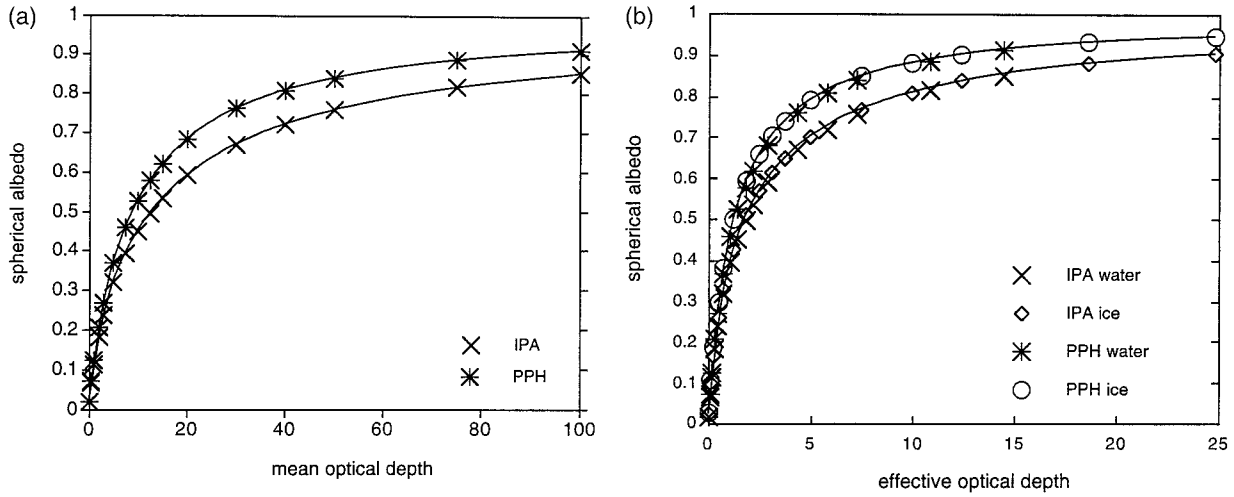

FIG. 1. (a) PPH and IPA visible spherical albedos for the ISCCP water droplet model as a function of the mean of 4096-long optical depth strings generated with the bounded cascade model of Cahalan et al. (1994a). (b) PPH and IPA visible spherical albedos for both the droplet and crystal ISCCP phase functions for the same strings used in (a), but as a function of effective optical depth $(1 - g)\tau$.

the PPH albedo found from the true mean optical depth is always greater than or equal to the IP albedo.

As conventionally defined, the IP albedo involves only one-dimensional, plane parallel calculations. That is, the individual pixels of the cloudy atmosphere are treated as plane parallel slabs and without any net horizontal flux of radiation between pixels. This means that the spatial arrangement of pixels is irrelevant (Stephens 1985), and no account is taken of any of the effects of 3D morphology. While the IP albedo seems reasonably accurate for some extended cloud layers (Cahalan et al. 1994b), its general accuracy remains debatable, and three-dimensional cloud effects may clearly dominate at high spatial resolution (Marshak et al. 1995a; Marshak et al. 1995b). However, such considerations go beyond the scope of this study, which addresses the difference between the PPH and IP albedos, termed the PPH albedo bias, over scales comparable to those of climate models.

Some limited measurements of the PPH bias have been made. Cahalan et al. (1994a) used surface microwave radiometer measurements during the First ISCCP Regional Experiment (FIRE) to infer liquid water path and found that the PPH bias varies diurnally with an overall value of 0.09. By extrapolating this result to global scales they estimated that the assumption of homogeneous stratiform marine clouds everywhere can easily cause model errors of ~8% in the global planetary albedo. Cahalan et al. (1995) showed plots of the mean diurnal variation of albedo bias weighted by cloud fraction (their ''fractal structure bias'') during the Atlantic Stratocumulus Transition Experiment (ASTEX), which was also inferred from ground-based microwave radiometry. They found that the PPH albedo bias over the cloudy portion was larger in ASTEX than in FIRE due to more complicated cloud structures in the Azores region during the summer. Barker et al. (1996) also provided estimates of the PPH albedo bias for 45 Landsat scenes containing marine boundary layer clouds. They found overall PPH albedo biases of 0.03 for overcast Sc scenes, 0.087 for broken Sc scenes, and 0.094 for scattered Cu scenes.

Cahalan et al. (1994a) comprehensively described how the albedo bias varies with the mean, variance, and higher-order moments of the optical depth distribution, and how bias estimates and corrections are simplified when the first two *logarithmic* moments of τ are considered. They also showed how the relative albedo bias (defined as the ratio of the PPH albedo bias to the PPH albedo) depends on solar zenith angle and single-scattering albedo. The bias is small for thin clouds because of the linearity of the albedo curve at small optical depths and also for very thick clouds because of albedo saturation (see Fig. 1a). Maximum PPH albedo bias values therefore occur for intermediate values of optical depth. Cahalan et al. (1994a) found that, except for thin clouds, the relative bias decreases as the sun moves toward the horizon (since each pixel becomes more reflective) and that the bias decreases more rapidly for thick clouds when scattering is nonconservative.

Our goal in this study is to extend the above examples, which were limited to specific cases, to a more extensive satellite dataset that is statistically more representative of the range of albedo bias and to place greater emphasis on the step that precedes the albedo bias calculations, namely, on the factors that determine the probability distribution functions (PDFs) of optical depth. We examine, for example, how the mean and variance of the retrieved PDFs depend on the method used to retrieve optical depth, the viewing–illumination geometry, the data resolution, etc. We focus on absolute (as opposed to relative) albedo bias since it is this quantity that is most directly linked to errors in solar energetics.

The next section describes the dataset used, our meth-

odology, and assumptions. Section 3 shows the magnitude of albedo bias as a function of region size and describes its dependence on various assumptions and the viewing–illumination geometry. Section 4 examines the effects of data resolution, while section 5 considers the biases from a GCM's perspective by examining grid-box-averaged albedo biases. We conclude with a summary and discussion in section 6.

2. Dataset and methodology

An extensive AVHRR local area coverage (LAC) dataset (1.1-km resolution at nadir) from the *NOAA-11* satellite was used in this study. The data were spatially restricted to a large region of the Atlantic Ocean from 9° to 45°N and 19° to 58°W, and covered the period August–October 1993 with only a few missing days. Since a complete AVHRR scan line (2048 pixels) was rarely confined within this region, only 300-pixel long segments centered around nadir (viewing zenith angles ~0°–9°), the middle of the two half-scanlines (~22°–42°), or the edges of the scanline (~46°–69°) were required to belong to the above domain. This approach maximizes the data available for analysis (it provided a total 1.5×10^8 pixels; 3×10^7 pixels near nadir) and facilitates detection of systematic τ and PPH bias differences among the various geometries. Each collection of consecutive scan line segments along the satellite path for a particular day was treated as a distinct data file (''scene'') in the albedo bias calculations. In the following, the segments will be referred to as ''nadir'' ''fsmv'' (forward scattering, medium views), ''fsov'' (forward scattering, oblique views), ''bsmv'' (backward scattering, medium views), and ''bsov'' (backward scattering, oblique views). The relative frequency of occurrence of solar zenith angles for each segment is shown in Fig. 2.

The calibration coefficients needed to convert channel 1 (Ch1; 0.63 μm) and channel 2 (Ch2; 0.86 μm) 10-bit counts to radiances were calculated following Teillet and Holben (1994) using updated tables for the period of interest (Di Girolamo 1995, personal communication). Clear and cloudy (assumed to be overcast) pixels were identified using the predetermined clear sky threshold (PCST) method of Di Girolamo and Davies (1995), which is a threshold method based on modeled variations of channel 2 reflectance over the ocean as a function of viewing and illumination geometry. Pixels that could have been affected by sun glint were also required to be ''cold enough.'' That is, their channel 4 brightness temperature had to be at least 7 K lower than the central value of the warmest 2-K-wide bin of the scene (provided it had least 1000 pixels). The retrieval of channel 1 cloud optical depth was accomplished with the aid of look-up tables constructed with the DISORT program of Stamnes et al. (1988), which is based on the discrete ordinate method solution of the radiative transfer equation. The C.1 water cloud model of Deirmendjian (1969)

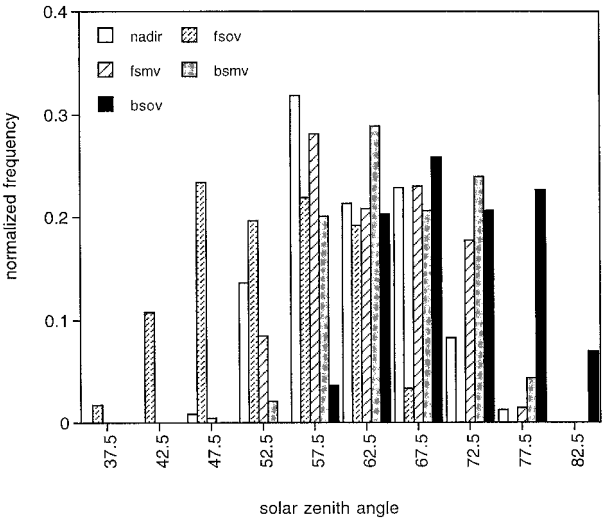

FIG. 2. Normalized frequency of occurrence of pixels with solar zenith angle within 5° bins for the different segments of the AVHRR scan line.

(effective radius $r_e = 6$ μm and asymmetry factor $g = 0.855$) was used (unless otherwise stated), clouds were assumed to occur in single layers and pixels to be radiatively independent (i.e., pixel radiance depends only on local pixel optical depth). Two kinds of radiance look-up tables were constructed: in the first, all atmospheric effects were neglected; in the second, scattering and absorption by the gases and aerosols of a standard maritime atmosphere were included by inverting 0.63-μm transmittances generated with LOWTRAN 7 (Kneizys et al. 1988). As discussed by Loeb (1992), use of monochromatic instead of narrowband (i.e., integrated over Ch1 response function) calculations introduces only a minimal error (~3%). The albedo of the ocean surface was assumed to depend on solar zenith angle in the manner depicted by Masuda (1991). A more detailed account of the optical depth retrieval procedure is provided by Oreopoulos (1996).

The retrieval method described above is conventional (e.g., Rossow and Schiffer 1991; Harshvardhan et al. 1994; Loeb and Davies 1996), and satisfies our objective of obtaining a first-order correction to the PPH albedo, bringing it closer to the IP albedo. Given the lack of detailed information on the atmospheric state, there may be errors in such an approach that are hard to assess. Where the errors are correlated, they will tend to cancel when the IP and PPH albedos are differenced to obtain the PPH bias. However, the accuracy of the IP albedo itself is limited by the potential influence of three-dimensional cloud morphology, ice crystal phase function, and multilayered cloud effects, and additional corrections will be appropriate in the future once these issues are better understood. Pixel albedos for the retrieved optical depths were also calculated at 0.63 μm from look-up tables constructed with DISORT. The PPH albedo bias B of a region was calculated from

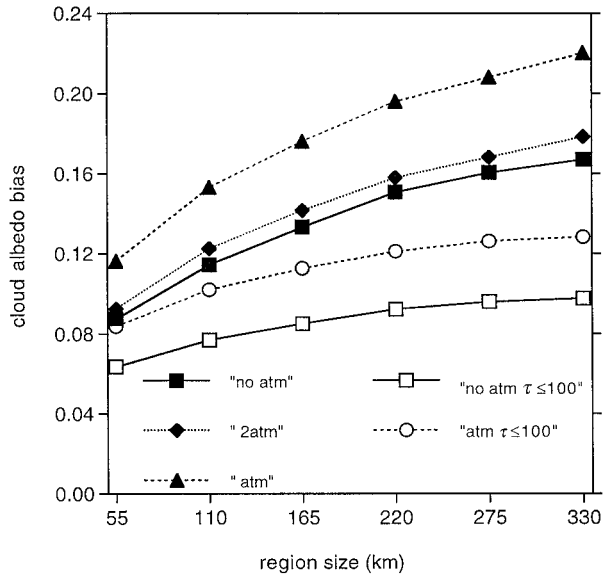

FIG. 3. Average channel 1 (Ch1) cloud albedo bias from Eq. (2) as a function of region size when no atmospheric effects are included in the optical depth retrieval algorithm (no atm), when atmospheric effects are considered for optical depth retrievals only (atm), and when atmospheric effects are considered for both optical depth retrievals and albedo calculations (2atm). Also shown are the cases where optical depths are set to a value of 100 in all albedo calculations whenever $\tau > 100$ for the no atm and atm datasets.

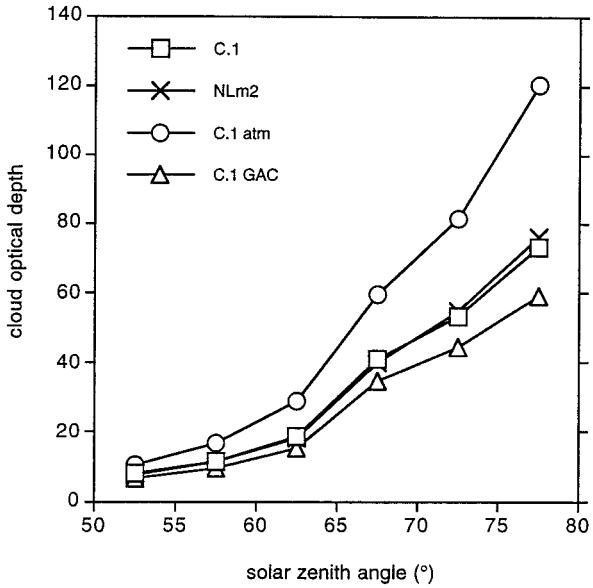

FIG. 4. Average Ch1 cloud optical depth as a function of solar zenith angle derived from the pixel-level values for the cases of a C.1 cloud model with (C.1 atm) and without (C.1) atmospheric effects included in the retrieval, the case of Loeb's (1992) microphysical model no2 (NLm2), and the case where LAC radiances are degraded to GAC resolution (C.1 GAC).

$$B = R(\overline{\tau}, \theta_0) - \frac{\sum_{n=1}^{N} R_n(\tau_n, \theta_0)}{N}, \quad (1)$$

where $\overline{\tau} = (\Sigma_{n=1}^{N} \tau_n)/N$ is the mean optical depth of the region (computed from the N cloudy pixels of the region), R is the plane parallel albedo, and θ_0 is the solar zenith angle (which varies very little within the region). The first term in the rhs of (1) is the PPH albedo and the second term the IP albedo. We calculated B for regions of different size, namely, arrays of $(50)^2$, $(100)^2$, $(150)^2$, $(200)^2$, $(250)^2$, and $(300)^2$ pixels corresponding to areas of $(55)^2$, $(110)^2$, $(165)^2$, $(220)^2$, $(275)^2$, and $(330)^2$ km^2 at nadir, respectively. Note that the same number of pixels corresponds to areas of different size at off-nadir views. With the exception of section 3c.(2), all results are from the nadir dataset.

3. Effects of assumptions and geometry

a. Atmospheric effects

Figure 3 shows the average albedo bias for the nadir segment as a function of region size, calculated from

$$\hat{B} = \frac{\sum_{m=1}^{M} B_m}{M} \quad (2)$$

where M is the number of regions of given size that contain some cloud and B_m is calculated from Eq. (1). We distinguish between three methods of calculating the PPH biases: ''no atm'' ignores the effects of the atmosphere above the cloud top on both the retrieval of cloud optical depth and the calculation of the bias; ''atm'' includes the effect of the atmosphere above the cloud in the retrieval of cloud optical depth and then calculates the PPH bias at the cloud top; ''2 atm'' is similar to atm but calculates the PPH bias at the top of the atmosphere, including the effects of the atmosphere above the cloud on radiation reflected by the cloud. The cloud is assumed to extend vertically from 2 to 3 km in a standard maritime LOWTRAN 7 atmosphere for both the atm and 2 atm cases. The PPH biases for the atm and no atm are thus for a cloud in a ''vacuum'' above a black surface (as in Cahalan et al. 1994a; Barker et al. 1996).

The biases for both no atm and atm cases show the expected upward trend, as clouds are assumed to be homogeneous over progressively larger scales, but the atm bias is significantly higher than the no atm bias, suggesting that the effects of the atmosphere are not entirely eliminated when albedo differences are taken. This can be explained with the aid of Figs. 4 and 5, which show that the two prime factors that control the bias, the mean and the variance of optical depth, are significantly higher in the atm case. Both increases are interrelated and can be understood by plotting nadir radiance as a function of cloud optical depth from the DISORT look-up tables (Fig. 6). The atmosphere becomes a net attenuator at Ch1 wavelengths when its effect is included between a reflecting surface (cloud)

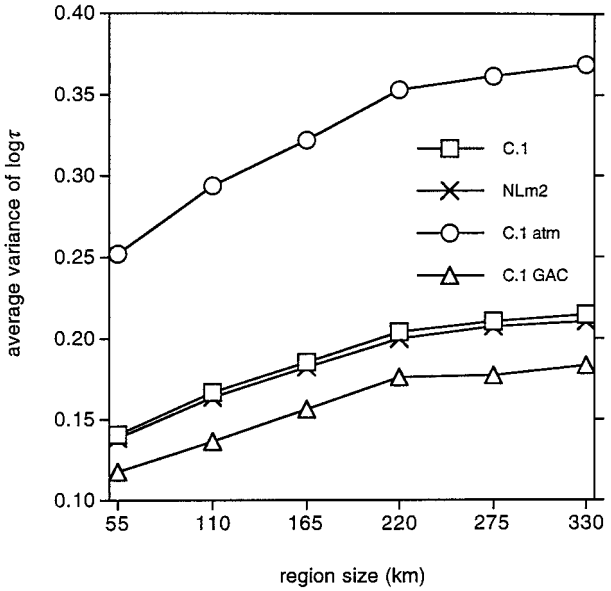

FIG. 5. Average Ch1 variance of logτ as a function of region size for the four cases depicted in Fig. 3. Here, logτ was calculated within each region from the cloudy pixel values and then averaged as in Eq. (2).

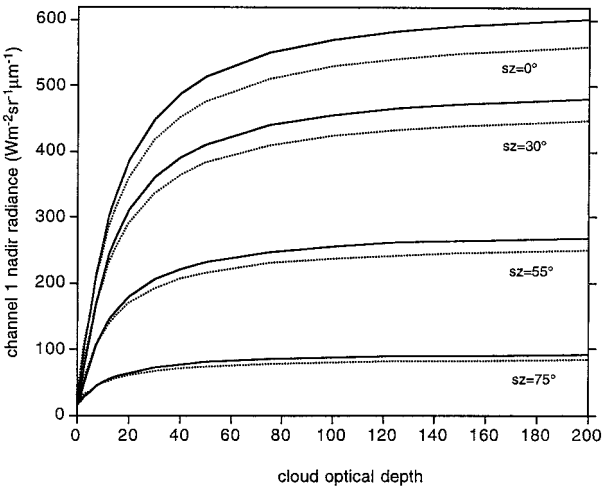

FIG. 6. Ch1 nadir radiance as a function of cloud optical depth for various solar zenith angles. The data are taken from the DISORT look-up tables. Solid curves are calculations with no atmospheric effects, while dotted curves include atmospheric effects.

and a sensor. This is because of ozone absorption (e.g., Saunders and Edwards 1989) and also molecular and aerosol scattering for sufficiently bright clouds (Hanan et al. 1995). For the solar zenith angles of the nadir segment (Fig. 2) this occurs mainly when $\tau > 10$. When accounting for atmospheric attenuation, larger cloud optical depths are needed to match the observations. Accounting for atmospheric effects also increases the apparent variability of the cloud optical depth fields. This again can be explained with the aid of Fig. 6. First, the atm curves have reduced curvature compared to the no atm curves, so that a greater τ difference corresponds to the same radiance difference. Second, more optical depths of the atm compared to the no atm category are located at the flat segment of the radiance curves where the sensitivity to radiance changes is the largest. Note also that the radiance change with optical depth becomes progressively smaller as solar zenith angle increases, so the differences in optical depth and variance between no atm and atm are expected to be more prominent at low Sun.

The magnitude of the PPH biases shown here implies large errors in TOA energetics for the homogeneous cloud assumption. At the scale of (55 km)^2 the bias is of the same order as that found by Barker et al. (1996) for broken Sc and scattered Cu (58 km)^2 scenes. However, a large contribution to the albedo bias comes from pixels with $\tau > 100$. As discussed in section 3c.(1), very large optical depth values are occasionally retrieved when $\theta_0 \geq 65°$. When an upper limit of 100 is imposed to the optical depth values (this affected ~2.5% of the pixels for the no atm and ~4% for the atm dataset), the albedo biases drop substantially (Fig. 3 "$\tau \leq 100$"), especially for the large region sizes. The reason is that limiting the optical depth significantly affects the mean optical depth value of a region, and hence its PPH albedo, but has only minimal effect on the IP albedo since pixel albedo is already near saturation at $\tau \approx 100$.

Interestingly, when atmospheric effects above the cloud are also included in the albedo calculations (curves 2atm of Fig. 3)—that is, when the albedo bias refers to the TOA and not the cloud top—the attenuation effects of the atmosphere bring the bias down to values slightly above the no atm case. Also note that the average biases weighted by regional cloud fraction $A_c = N_{\rm cld}/N$ ($N_{\rm cld}$ = number of cloudy pixels, N = total number of pixels in the region), namely,

$$\hat{B}_{\rm CF} = \frac{\sum_{m=1}^{M} A_{cm} B_m}{\sum_{m=1}^{M} A_{cm}}, \tag{3}$$

are qualitatively very similar to the biases of Fig. 3 (they are about 0.01 smaller) and are not shown.

b. Cloud model

Platnick and Valero (1995) and Han et al. (1994) have shown that AVHRR channel 1 reflectances are relatively insensitive to the effective cloud drop radius (r_e) of the assumed cloud model. In this section, we examine whether the expected insensitivity of the albedo bias to cloud microphysics (for water clouds) is consistent with our calculations. We test this by comparing the results for the C.1 cloud model, which has $r_e = 6$ μm, with the results for Loeb's (1992) cloud model 2 (NLm2),

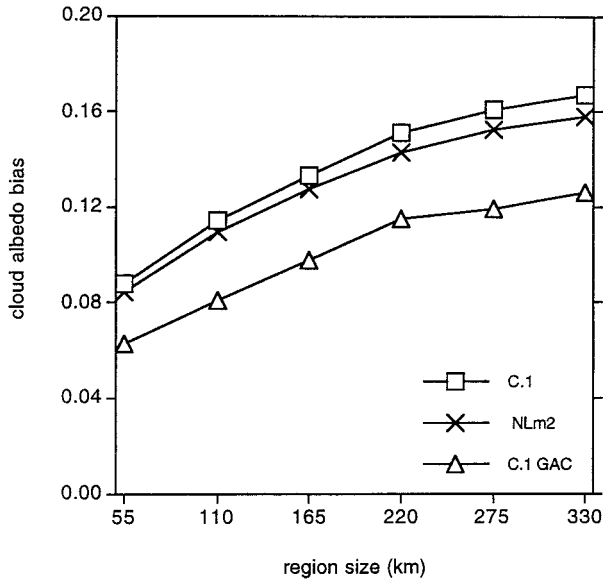

FIG. 7. Average Ch1 albedo bias from Eq. (2) as a function of region size for three of the cases of shown in Figs. 3 and 4.

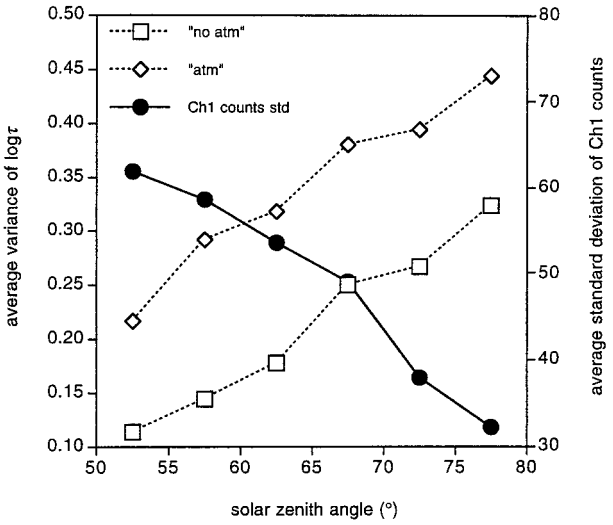

FIG. 8. Average variance of Ch1 logτ, for both the atm and no atm cases, and average Ch1 standard deviation of the raw measurements as a function of solar zenith angle, for (165 km)^2 areas.

which has $r_e = 12$ μm. The proximity of the two bias curves in Fig. 7 (they differ by less than 0.01) comes as no surprise since the mean optical depth and variability values are almost identical, as shown in Figs. 4 and 5. The similarity of the retrieved τ fields for the two microphysical models is due to the conservative nature of scattering at visible wavelengths whereby changes in effective radius can influence cloud reflectance only via changes in the phase function. The phase functions of the two cloud models (not shown) are very similar ($g = 0.855$ for the C.1 model and $g = 0.865$ for the NLm2 model). Had an ice crystal phase function with smaller asymmetry parameter been used (Takano and Liou 1989; Mishchenko et al. 1996), the retrieved τ values would have been smaller, but (given our extensive sampling of scattering angle) the distributions of effective optical depth $(1 - g)\tau$ would have been similar to those for a droplet model. Figure 1b shows that the effects of cloud microphysics on albedo are second order, provided the albedo is calculated using the effective optical depth, and consequently there is little change in the bias calculations, irrespective of whether the clouds are liquid or ice. However, while microphysics is relatively unimportant when PPH biases are calculated from the inversion of visible radiance measurements, it has a stronger influence when optical depths are inferred from measurements of water path W using $\tau = 3W/2\rho r_e$ (as in Cahalan et al. 1994a).

c. Geometric effects

1) SOLAR ZENITH ANGLE

Figure 4 showed that the retrieved cloud optical depth varies systematically with solar zenith angle for near-nadir observations. Despite the uneven sampling of solar zenith angle (Fig. 2), the increase in optical depth is too systematic to be fortuitous. Loeb and Davies (1996) observed the same behavior in coarser-resolution ERBE data and explained it by noting that the nadir reflectance was sensitive to both side illumination and nonflat cloud tops, neither of which are accounted for by the current 1D retrieval of optical depth. Figure 8 shows that the average variance of logτ also increases with solar zenith angle despite the decrease in the average standard deviation of the Ch1 raw measurements. The results plotted in Fig. 8 are for (165 km)^2 (i.e., 150 $\times$ 150 pixels) areas, but similar behavior is also noted for the other areas. The increase in average logτ variance with sun angle appears to be the outcome of interpreting observed radiances with plane parallel models (Fig. 6): since relatively large τ values are retrieved at low sun and since the radiance curve is flat under these conditions, even small radiance (I) increments can lead to large increases in retrieved optical depth. In other words $d\tau$ at low sun is larger than $d\tau$ at high sun for the same dI.

Given the trends of Figs. 4 and 8, the general increase in PPH bias with sun angle (Fig. 9) is not surprising. The upward trend, however, ends before the last solar zenith angle bin because large optical depths, with saturated albedos, are very frequently retrieved at the most oblique angles. The behavior shown in Fig. 9 for (165 km)^2 areas is also observed for the other areas and is due to the fact that the albedos are calculated at the same solar zenith angles at which the optical depths are retrieved. When the PPH biases of the current optical depth distributions are calculated at arbitrary solar zenith angles, the angle dependence is different. This is shown in Fig. 10, where the average PPH bias is plotted for the full range of solar zenith angles. The albedo bias shows a tendency of slight increase up to about 55° for

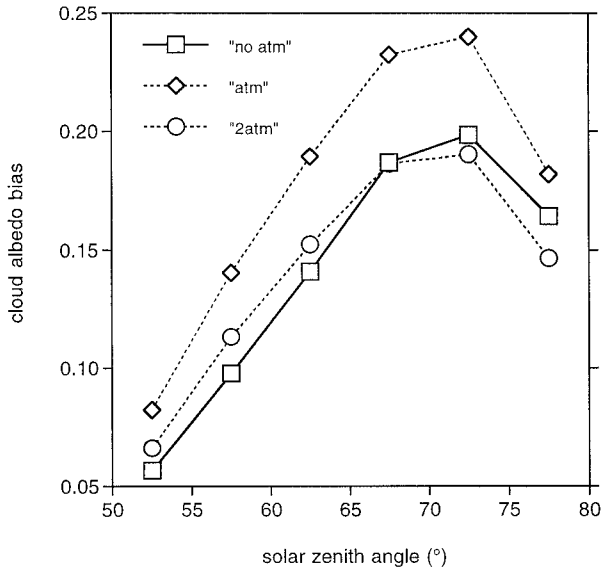

FIG. 9. Average (165 km)^2 Ch1 cloud albedo bias as a function of solar zenith angle for three of the cases shown in Fig. 4.

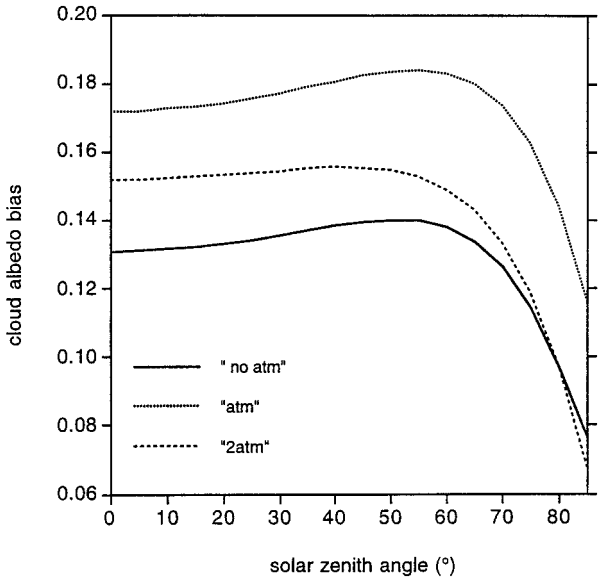

FIG. 10. Average Ch1 cloud albedo bias as a function of solar zenith angle for (165 km)^2 areas, when albedos are calculated for the full range of solar zenith angles (and not only for the angles at which the optical depths are retrieved). The three cases shown are the same as in the previous figure.

both the no atm and atm cases and a fast drop after about 70° due to the rapid brightening of pixels at oblique sun. Figure 10 does not, of course, depict the universal dependence of cloud albedo bias on solar zenith angle, but the specific dependence corresponding to the present AVHRR optical depth distributions.

A ''spherical'' PPH bias can be obtained by integrating the biases plotted in Fig. 10 over the complete range of solar zenith angles, namely,

$$B = 2\int_0^1 \mu'\hat{B}(\mu')\,d\mu'. \tag{4}$$

These albedo biases differed by less than 0.005 from the directional albedo biases plotted in Fig. 3 for all cases and region sizes.

2) VIEWING ANGLE AND RELATIVE AZIMUTH

Examination of the different view angle segments of the data shows (Fig. 11a) a systematic increase in PPH bias from oblique forward scatter to oblique backscatter, with the average bias increasing with region size for each segment. This behavior is consistent with a similar increasing trend in the variance of $\log\tau$ from forward to backward scatter.

This behavior is probably due to the solar zenith angle sampling within each segment (Fig. 2). Clearly, the backscattering segments are associated with larger solar zenith angles than the forward-scattering segments. The saturation of albedo expected at the most oblique sun angles does not appear to compensate for the general increase in the frequency of optical depths belonging to the high curvature segment of the $R(\tau)$ curve and the apparent increase in variability. Note that due to uneven solar angle sampling it was unclear whether each segment had its own solar zenith angle range in which optical depths increased with θ_0 in a manner similar to the nadir case. For example, it was found that at the very large (backscattering) and relatively small (forward scattering) solar zenith angles, the mean optical depth of the oblique view segments did not follow the monotonic increase shown in Fig. 4.

Subsequently, we attempted to remove the effect of solar zenith angle in the segment comparison by selecting solar zenith angle bins where each segment had at least 10^6 pixels. Only two bins satisfied this criterion, 55°–60° and 60°–65°. Figure 12 shows the results for 150 pixel × 150 pixel arrays. The average bias and logarithmic variance of the 55°–60° bin follow the same increasing trend as the all-angle results of Fig. 11. However, there is significant sampling bias: the bsov results are based on only 54 arrays with the standard deviation of the mean reaching 0.02, while standard deviations for the other segments are at least three times smaller. The other bin, which has more uniform sampling (the standard deviation of the mean is always below 0.008), shows the expected increase in apparent uniformity with view angle (Davies 1994) only for the backscattering direction. Thus, from these results it is not possible to be conclusive on view angle dependence. In addition to radiance inversion with plane parallel models, sampling problems, possible ice cloud contamination, and pixel area expansion make a comprehensive interpretation difficult. The only clear tendency revealed by the off-nadir plots is that in the backscattering direction average bi-

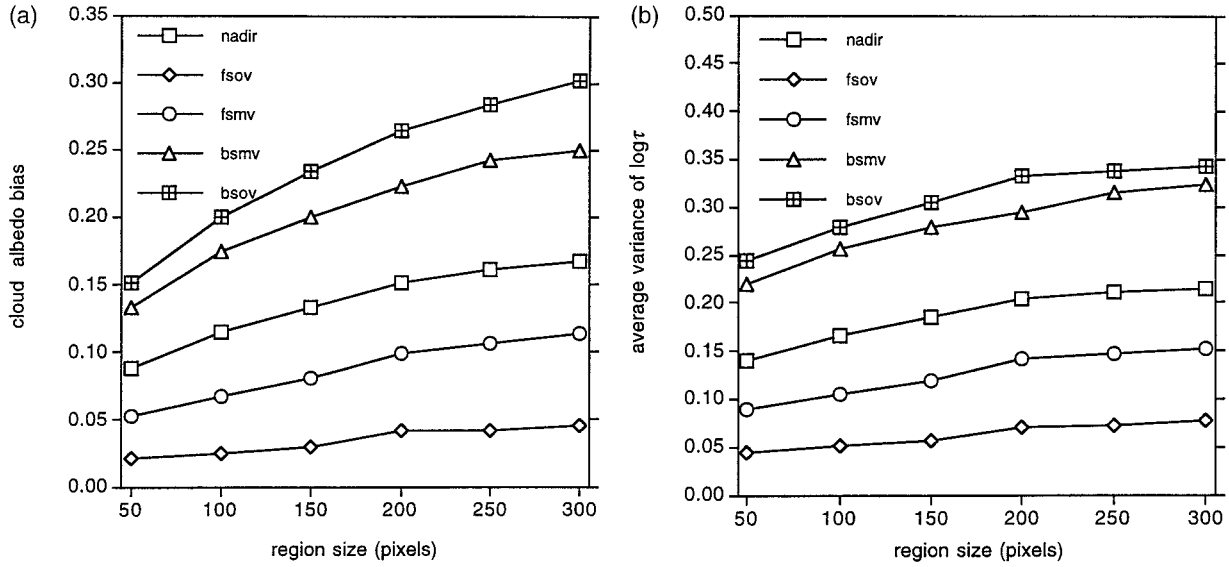

FIG. 11. (a) Average Ch1 no atm PPH bias calculated from Eq. (2) for the various segments of the AVHRR scan line as a function of region size in pixels. (b) As in (a) but for the variance of logτ.

ases are higher than those at nadir and the forward-scattering direction.

When area expansion with view angle is taken into account, fewer pixels are needed at off-nadir views to cover the same area as the corresponding nadir pixel arrays (Frulla et al. 1995). Using the pixel width and length expansion data of Oreopoulos (1996), we computed the bias from Eq. (2) for regions composed of the appropriate number of pixels along both the scan line and the satellite swath so as to preserve the nadir areas while maintaining their square shape. Substantial changes (decreases) in both PPH bias and logarithmic variance compared to the corresponding equal pixel array values occurred only for the oblique view segments (not shown). The bsov segment was influenced the most and its values actually dropped below those of the bsmv segment. The drop in these segments takes place because of the significant change in the number of pixels contributing to the variability within each region (pixel area increases by a factor ~10 at the edges of the scanline).

4. Resolution effects

If the resolution of the satellite measurements affects retrieved fields of optical depth to a significant extent, it should also affect the albedo bias estimates. Intuitively, we expect the apparent variability of cloud fields to

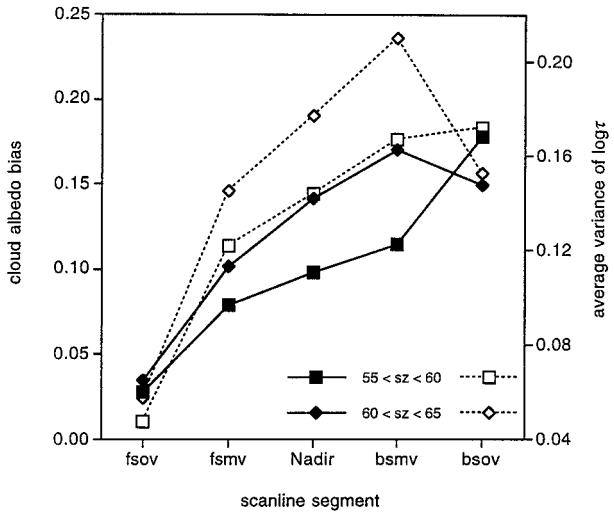

FIG. 12. Average Ch1 no atm PPH bias (solid curves) and variance of logτ (dashed curves) as a function of position on the AVHRR scan line for 150 pixel × 150 pixel arrays and the two solar zenith angle bins shown in the legend.

TABLE 1. Specifications for the six Landsat scenes used in this study.

Scene	Date	Lat/Lon (°)	Time UTC	θ_0	Cloud type
12	2 Aug 1985	32.73°N/121.45°W	1810	32°	Solid Sc
38	30 Jun 1990	33.19°N/21.42°W	1129	28°	Scattered Cu
39	4 Jul 1990	33.19°N/15.26°W	1104	28°	Solid Sc
40	5 Jul 1990	36.06°N/25.27°W	1146	29°	Scattered Cu
43	8 Jul 1990	33.18°N/33.81°W	1218	28°	Broken Sc
49	14 Jun 1992	33.18°N/16.75°W	1115	32°	Scattered Cu

be smaller when they are observed with coarse-resolution sensors or when high-resolution measurements are degraded to lower resolution. Furthermore, mean optical depth values may also be affected by the resolution of the satellite data because pixels are commonly assumed to be homogeneous. First, the neglect of subpixel cloud fraction introduces underestimates of cloud optical depth, which grow with pixel size, since larger pixels are more often partially cloudy. The lower values of optical depth retrieved in this case are explained by the reduction in the average reflected radiance from the clear portion of the pixel (''cloud fraction effect''). Second, the radiance from the cloudy portion of the pixel has a nonlinear dependence on optical depth (Fig. 6), so that inversion of the average cloudy radiance does not give the mean cloud optical depth of the pixel, but some lower value (''nonlinear averaging effect''). This effect, of course, applies even to overcast pixels and is also expected to increase with pixel size since cloud inhomogeneity is likely to be greater for larger pixels.

This section examines the PPH bias for resolutions both coarser and finer than LAC. To study the effects of reduced resolution, the LAC data are degraded to the global area coverage (GAC) resolution, a standard used for storage of global AVHRR datasets. Two different methods are used to compare biases from LAC and higher resolution measurements: 1) high-resolution Landsat scenes are assumed to be viewed by the AVHRR instrument, and 2) the resolution of LAC is enhanced by a factor of 4 with the aid of a stochastic method that uses the observed slope of the radiance power spectrum at small scales.

a. LAC versus GAC

Ch1 and 2 LAC counts for the nadir segment were reduced to GAC resolution by averaging 4 out of 5 pixels along the scan line for every third scan line. Pixel homogeneity was then invoked again, and the PCST thresholds were used to classify GAC pixels into clear and overcast. Optical depth retrieval and albedo bias computations remained as before. The average albedo bias for GAC as a function of region size is shown in Fig. 7. There is a substantial drop ($\approx$0.02–0.05) in the computed albedo bias compared to LAC. This is the combined effect of the reductions in retrieved optical depth (Fig. 4) and logarithmic variance (Fig. 5).

b. Landsat versus LAC

Six Landsat scenes containing marine boundary layer clouds (three scattered Cu, one broken Sc, and two overcast Sc) were available for analysis (see Table 1). Each scene consisted of $(2048)^2$ 28.5 m pixels. The names of the scenes follow Harshvardhan et al. (1994). Reflectance thresholds for pixel classification were set with the aid of image processing software (Di Girolamo 1995, personal communication). Optical depths at 0.83 μm were computed in a manner similar to that of AVHRR, and the NLm2 cloud model was used with no atmospheric effects included in the retrieval (as in Harshvardhan et al. 1994). Analysis was simplified by the fact that the thematic mapper (TM) radiometer aboard the Landsat satellite observes at nadir. However, one should also be conscious of the problems inherent in the analysis of this high-resolution dataset: first, the TM radiometer, which was not designed to observe clouds, has a low dynamic range (saturates easily); and second, the IPA, which is invoked in the optical depth retrievals, is probably not valid at such small scales. Discussion on the latter problem can be found in Barker (1996), Marshak et al. (1995a,b), and Oreopoulos (1996). To simulate LAC measurements, we averaged the radiances of 40 $\times$ 40 pixel arrays and proceeded to pixel classification and optical depth retrieval as before (assuming again LAC pixel homogeneity).

Reduction to LAC resolution had a significant impact in four of the six scenes (Fig. 13): The overcast stratocumulus scenes (12 and 39) were quite homogeneous and their albedo biases remained almost unchanged. On the other hand, the assumption of pixel homogeneity for the simulated LAC data made the broken clouds appear much thinner and drastically reduced their albedo bias. Scene 43 is very heterogeneous with thicker clouds than the Cu scenes and is the only one with albedo bias at LAC resolution comparable to that shown in Fig. 3 for the $(55\ \text{km})^2$ area size. The large increase in the cloud fraction of the Cu scenes upon reduction to LAC resolution (shown in Oreopoulos 1996) implies that the substantial drop in PPH bias is mainly due to the cloud fraction effect. This conclusion is also supported by estimates of the average PPH bias within simulated LAC pixels, which does not exceed 0.01 for any scene (as shown in Oreopoulos 1996). Since broken marine boundary layer clouds are usually intermittent and have

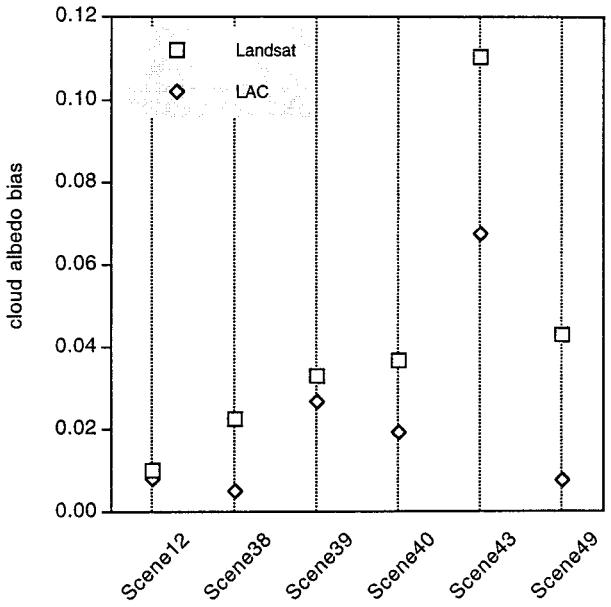

FIG. 13. The 0.83-μm cloud albedo bias for six of the Landsat scenes in Harshvardhan et al. (1994) at the original TM resolution (28.5 m) and when the data are degraded to LAC resolution.

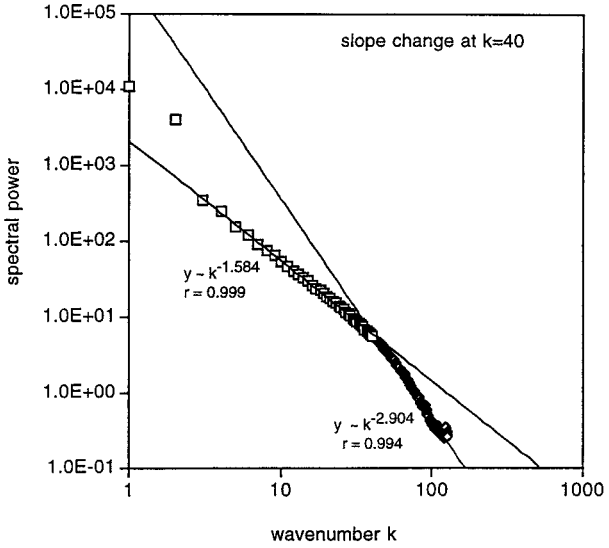

FIG. 14. Ensemble-averaged 1D power spectrum for the Ch1 counts of the nadir dataset. Due to the use of the fast Fourier transform algorithm only 256 pixels centered at the subsatellite point were used per scan line. To convert from wavenumber to length (in km) simply use $256 \times 1.1/k$.

cell sizes smaller than LAC pixels, the results shown here probably represent the upper limit of bias reduction upon resolution coarsening. On the other hand, the PPH bias for scene 12, which is extremely homogeneous, probably represents the low limit of the nonlinear averaging effect.

c. Enhanced LAC

The original AVHRR Ch1 and Ch2 counts of the nadir segment were enhanced fourfold in resolution (to about 275 m) using a procedure developed by Várnai (1995, personal communication) that generates random small-scale variations, which follow a power-law scaling. This method is based on the same principle as the method used by Várnai (1996) to produce stochastic arrays of clouds (which in turn is a variation of the method of Barker and Davies 1992a). A description of the procedure can be found in Oreopoulos (1996). The power spectrum slope of the radiance field required by Várnai's code was determined from the observations. For computational efficiency, the fast Fourier transform algorithm was used to calculate the radiance power spectrum of the nadir segment. Since this algorithm requires the number of points to be 2^n, only 256 pixels centered at the subsatellite point were used per scan line. Figure 14 shows the Ch1 1D ensemble-averaged power spectrum (the Ch2 power spectrum is very similar). The power spectrum is very smooth, because of the large number of scan lines used, and has a distinct spectral slope break at wavenumber $k \sim 40$ (which corresponds to about 7 km). Such breaks also occurred in the satellite power spectra presented by Barker and Davies (1992b), Barker (1996), and Cahalan and Snider (1989). The slope before the break is close to $-5/3$, suggesting isotropic turbulence at large scales, while following a ~ -3 power law at smaller scales, indicating a rapid fall off in variability. We assumed that the power scaling law for $k > 40$ also applies at scales smaller than the Nyquist frequency (2 pixels = 2.2 km) and thus used the -3 spectral slope to enhance 357 (256×256) scenes belonging to the nadir segment by a factor of 4.

The average PPH bias for areas corresponding to 64×64, 128×128, and 256×256 (original resolution) pixel arrays was calculated at the original and enhanced resolutions (the latter have 16 times more pixels than the number indicated above). We also averaged the radiances obtained by the enhancement routine back to the original resolution. We call this the ''degraded'' dataset. The biases for the enhanced scenes should be thought of as the biases that would be computed if the scenes were observed by a radiometer with resolution four times higher than AVHRR. Accordingly, the biases resulting from the degradation of the enhanced scenes should be thought of as the biases that would be obtained if the enhanced scenes were observed by the 1.1-km AVHRR radiometer—that is, a radiometer that cannot resolve all existing cloud variability. Figure 15 shows that the average biases of the original (squares) and enhanced resolution (diamonds) images are virtually identical for both the no atm (lower curves) and atm cases (upper curves). This implies that the rapidly decaying variability at small scales is unable to produce substantial nonlinear averaging effects on an average basis. Note that in this comparison there is no cloud fraction effect because we assume that the enhanced

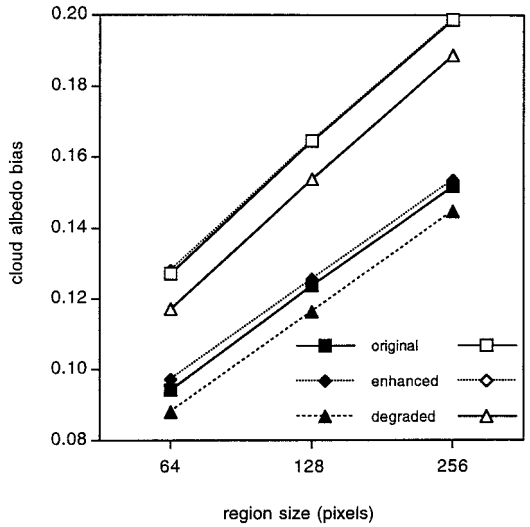

FIG. 15. Average Ch1 albedo bias for three different region sizes (in pixels). Solid symbols are for no atm optical depths and open symbols are atm optical depths. The three curves of each set are explained in the text.

resolution ''scenes'' are viewed by an equivalent resolution radiometer. In contrast, when the enhanced fields are assumed to be viewed by the AVHRR instrument (counts of 4×4 pixels are averaged), cloud fraction effects are also present and produce a discernible reduction of ~ 0.01 in the PPH bias (circles). Thus, the above exercise suggests that if subpixel cloud fraction is known for sufficiently small pixels (such as LAC pixels), the average PPH bias can be calculated with relatively high accuracy, even when liquid water variations within the cloudy part of the pixel are not resolved. If, on the other hand, the cloud fraction is unknown (as is usually the case), errors in the PPH bias can occur. It is worth noting that the results shown in Fig. 15 did not change when the -1.6 slope observed before the break was used in the enhancement routine. This suggests that only spectral slopes far less steep than the ones observed here can have a significant impact on PPH biases, for a fourfold enhancement in resolution.

How realistically Várnai's routine simulates subpixel cloud variations is unknown. It should be noted that locally, the PPH bias differences among the three cases of Fig. 15 become significantly larger than the differences of the average values. This is not surprising considering the random nature of the artificially generated small-scale variations and the dependence of the bias on mean optical depth. In the real world, however, small-scale variations do not always follow the steep power-law scaling, which was universally applied here to get the enhanced fields. This conclusion seems to be supported by the substantial difference in the PPH biases between the LAC and GAC resolutions and the occasional existence of large internal PPH biases in LAC-size pixels simulated from Landsat data (as noted by Oreopoulos 1996). Clearly, only when high-resolution radiometric data become routinely available will we be in a position to examine more effectively resolution effects on PPH bias.

5. All-sky albedo bias

The preceding analysis addressed the albedo bias of only the cloudy portion of each region. However, for GCM's capable of predicting cloud fraction and cloud water in each grid box, a more appropriate quantity may be a grid-box-averaged (''all-sky'') bias, which will be smaller than our original PPH bias for partially cloudy grid boxes. The reason is that clear regions similar in size to those considered have much more homogeneous radiative properties than the cloudy skies. Moreover, because of the small optical depths involved, clear sky reflectances follow linear averaging laws with greater precision. The all-sky bias would therefore be well approximated by the cloudy bias multiplied by the cloud fraction. Hereafter, this is called type 1 all-sky bias.

Still, most older GCMs, and some current ones, have no capability of predicting cloud fraction. Furthermore, even GCMs that have cloud fraction parameterizations (especially threshold relative humidity algorithms) tend to have either clear or overcast grid points at the individual time steps of the calculation. This has been documented for the Canadian Climate Centre GCMII (Barker 1995) but likely takes place in other GCMs as well (their qualitative agreement with observed cloud climatologies is often the result of canceling errors when averaging completely clear and overcast values). For this reason, it is insightful to calculate the bias resulting from homogeneously distributing the cloud mass over the *entire* region. This is hereafter named type 2 all-sky bias and is calculated from

$$B_{\text{type2}} = R(A_c\overline{\tau},\, \theta_0) - \frac{\sum_{n=1}^{K} R_n(\tau_n,\, \theta_0)}{K}, \qquad (5)$$

where $K = N/A_c$ is the total number of pixels in the region.

Since clear-sky albedos are included in the summation in (5), the biases shown in the following for both types of all-sky biases are ''column'' (TOA) biases. That is, albedo calculations include atmospheric effects above and below the cloud and take into account ocean surface reflectance. Note that for these calculations, the atm optical depths are used. Also note that neither of our type 1 or type 2 biases is the same as the ''total absolute bias'' of Cahalan et al. (1994a) defined by their Eq. (6.1). Our type 1 bias, however, is the same as the ''fractal structure bias'' defined by Eq. (4.2) of Cahalan et al. (1995), while what these papers refer to as ''cloud fraction bias'' is the difference between our type 1 and type 2 biases.

Figure 16a shows the average type 1 and type 2 biases

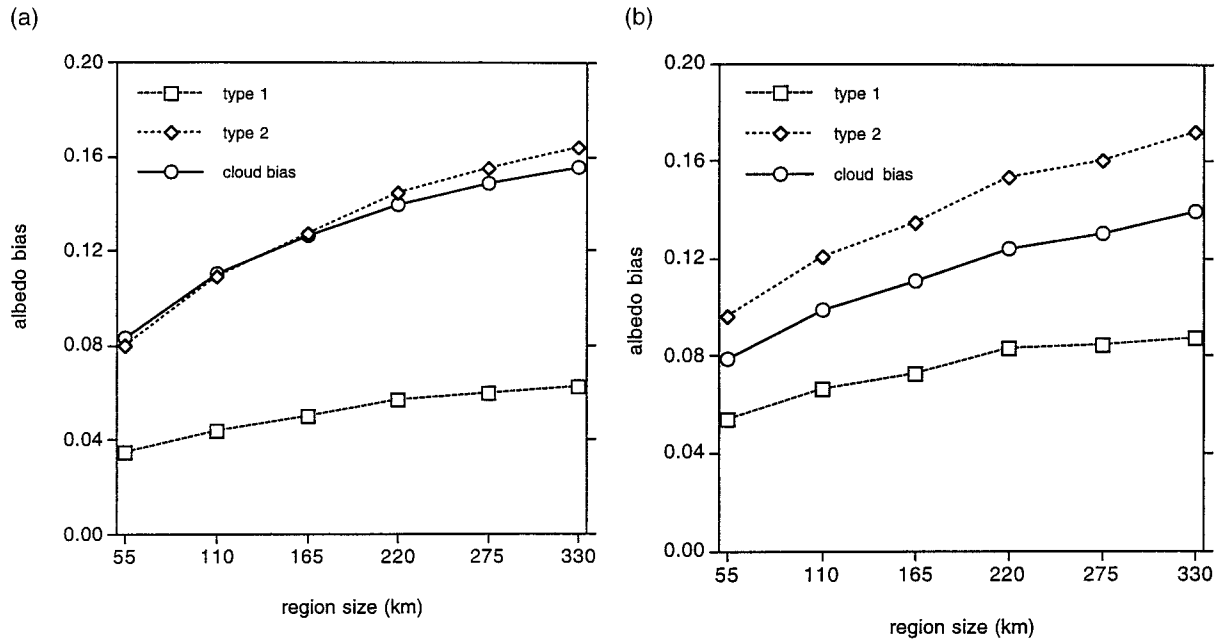

FIG. 16. (a) Average bias as a function of region size for the three cases described in the text. (b) As in (a) but only for regions having cloud fraction greater than 0.3.

along with the bias over the cloudy only portion of each region. All biases show the expected upward trend as homogeneity is assumed over progressively larger regions. The cloudy bias is similar to the 2 atm bias of Fig. 3. The type 2 bias is, as expected, much larger than the type 1 bias and is actually larger than the cloud PPH bias for large region sizes. Thus, GCMs with no subgrid cloud fraction have to scale down their cloud water even more in order to bring their albedos close to observations. Figure 16b shows a similar plot, but with only regions having $A_c > 0.3$ included in the averaging. This case can be considered to represent GCMs, which form clouds only after a significant accumulation of cloud water. Cloudy biases decrease not because regions with $A_c > 0.3$ are more homogeneous, but because they contain a greater proportion of the very thick (optically) clouds for which albedo is insensitive to optical depth variations. Type 1 biases increase despite the decrease in cloudy biases because of the large increase in the average cloud fraction.

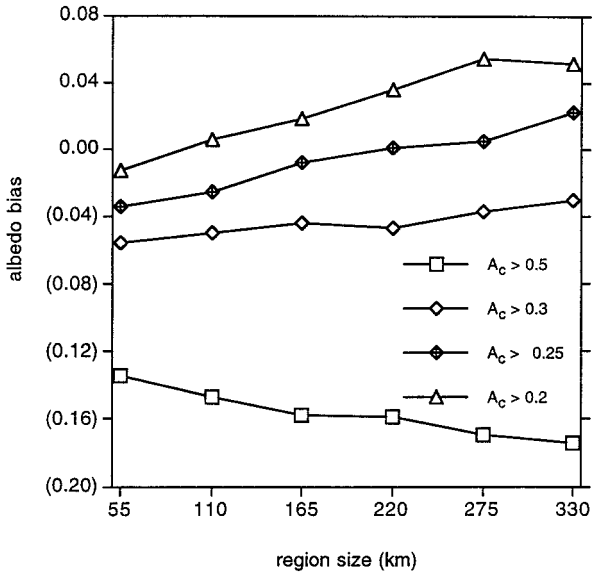

FIG. 17. Average ''overall'' all-sky bias as a function of region size for cloud fractions exceeding the thresholds shown in the legend.

The above results suggest large albedo biases in homogeneous GCM grid boxes. However, in model simulations these errors may be compensated by underestimates in albedo due to an excessive number of *clear* grid boxes compared to the real world. To recreate such a scenario with the current dataset, regions were assumed overcast when cloud fraction exceeded certain thresholds, while they were assumed completely clear when cloud fraction was below these thresholds. Then, the type 2 bias was calculated from Eq. (5) for the regions above the threshold, while for the regions below the threshold, a (negative) bias was calculated by replacing the first term in the rhs of Eq. (5) with the clear-sky albedo. When the latter bias was added to the type 2 bias, an ''overall'' bias was obtained. Figure 17 shows the average overall bias for various cloud fraction thresholds, namely, 0.5, 0.3, 0.25, and 0.2. For the 0.5 threshold, the underestimate in the clear regions overpowers the overestimate at cloudy regions by a large amount. As the threshold drops, the ''overall'' bias progressively changes sign. With the exception of the small-

est region size, the overestimates and underestimates cancel somewhere between the 0.3 and 0.2 cloud fraction thresholds. Thus, under certain conditions, albedo biases obtained from averaging over a large number of grid boxes can become small because of canceling errors. This example elucidates how climate models can arrive at realistic solar energy budgets on a global or even regional basis, in spite of totally unrealistic cloud water distributions. However, the instantaneous local errors at individual grid points may still be significant for some aspects of the GCM's climate.

6. Conclusions

We have calculated AVHRR 0.63-μm PPH albedo biases over a large portion of the North Atlantic. The average visible cloud albedo bias varied with scene size from $\approx$0.12 for $(55\ \text{km})^2$ scenes to $\approx$0.22 for $(330\ \text{km})^2$ scenes. This result is for the nadir segment of the AVHHR data, including atmospheric effects.

Biases were slightly lower if atmospheric effects were not included and were typically halved when evaluated over the entire region and not only the cloudy part. The off-nadir segments of the data showed highly variable biases, with highest values of $\approx$0.30 being obtained for the bsov segment [$(300)^2$ pixel regions] and lowest values of $\approx$0.02 being obtained for the fsov segment of the no atm dataset [$(50)^2$ pixel regions].

The bias results are limited by the plane parallel assumptions used in the independent pixel approximation. Because the retrieved cloud optical depths increase with increasing solar zenith angle, due in part to side illumination and in part to cloud-top morphology (see Loeb and Davies 1996), and perhaps also to ice crystal phase function effects, the retrieved biases also tend to increase with solar zenith angle. Similarly, subpixel heterogeneity also affects some of the IP retrievals of optical depth.

We also calculated broadband albedo biases using Slingo's (1989) scheme. Results were not shown here since they were qualitatively similar to those for AVHRR Ch1. Broadband biases were about 10% smaller than visible biases, while the biases in broadband absorptance were also positive and about 10% of the albedo biases (for $r_e = 6\ \mu$m).

The above values suggest that biases in the reflected solar flux can easily exceed 30 W m^{-2}. Thus, horizontal cloud homogeneity is a very poor assumption for areas similar in size to GCM grid boxes and can potentially generate radiation budget errors far larger than greenhouse gas induced forcings. Although climate models are tuned to produce the observed zonal variations of albedo by scaling their cloud water amounts down, advances in prognostic cloud representation will make more difficult the coexistence of realistic hydrological cycles and artificially low cloud liquid water contents.

In a companion paper, Oreopoulos and Davies (1998) use the same dataset to suggest ways to correct the PPH albedo bias. While these corrections substantially reduce the error in average scene albedo due to the PPH albedo bias, more thorough corrections will inevitably require a deeper consideration of three-dimensional cloud morphological effects. Such studies await the next generation of satellite data that should become available from the Earth Observing System. Together with the enhanced spatial resolution of the new sensors and improved treatment of multilayered clouds, the Earth Observing System plans (Wielicki et al. 1995) to include first-order corrections for three-dimensional cloud effects in its retrieval of cloud optical properties. These more accurate cloud optical depths should in turn be used to improve the estimates of the PPH albedo bias given here.

Acknowledgments. We thank Eugene Clothieux of The Pennsylvania State University and the U.S. Geological Survey's EROS Data Center for the AVHRR data, Bruce Wielicki of NASA LaRC and Lindsay Parker of Lockheed Eng. and Sci. Co. for the Landsat data, and Michael Mishchenko of NASA GISS for the ISCCP ice phase function. Thanks go to Bryan Baum of NASA LaRC for the code that unpacks the AVHRR data and to Howard Barker of AES/ARMP and the two anonymous reviewers for their suggestions toward improving the manuscript. This research was supported in part by grants from the Natural Sciences and Engineering Research Council and the Atmospheric Environment Service (Canada).

REFERENCES

Barker, H. W., 1995: Methodological dependencies of cloud radiative forcing for the Canadian Climate Centre second-generation general circulation model. *J. Geophys. Res.,* **100,** 1017–1025.

——, 1996: A parameterization for computing grid-averaged solar fluxes for inhomogeneous marine boundary layer clouds. Part I: Methodology and homogeneous biases. *J. Atmos. Sci.,* **53,** 2289–2303.

——, and J. A. Davies, 1992a: Solar radiative fluxes for stochastic, scale-invariant broken cloud fields. *J. Atmos. Sci.,* **49,** 1115–1126.

——, and ——, 1992b: Cumulus cloud radiative properties and the characteristics of satellite radiance spectra. *Remote Sens. Environ.,* **42,** 51–64.

——, B. A. Wielicki, and L. Parker, 1996: A parameterization for computing grid-averaged solar fluxes for inhomogeneous marine boundary layer clouds. Part II: Validation using satellite data. *J. Atmos. Sci.,* **53,** 2304–2316.

Cahalan, R. F., and J. B. Snider, 1989: Marine stratocumulus structure. *Remote Sens. Environ.,* **28,** 95–107.

——, W. Ridgway, W. J. Wiscombe, T. L. Bell, and J. B. Snider, 1994a: The albedo of fractal stratocumulus clouds. *J. Atmos. Sci.,* **51,** 2434–2455.

——, ——, ——, S. Gollmer, and Harshvardhan, 1994b: Independent pixel and Monte Carlo estimates of stratocumulus albedo. *J. Atmos. Sci.,* **51,** 3776–3790.

——, D. Silberstein, and J. B. Snider, 1995: Liquid water path and plane-parallel albedo bias during ASTEX. *J. Atmos. Sci.,* **52,** 3002–3012.

Davies, R., 1994: Spatial autocorrelation of radiation measured by

the Earth Radiation Budget Experiment: Scene inhomogeneity and reciprocity violation. *J. Geophys. Res.,* **99,** 20 879–20 887.
Deirmendjian, D., 1969: *Electromagnetic Scattering of Spherical Polydispersions.* Elsevier, 290 pp.
Di Girolamo, L., and R. Davies, 1995: The imaging navigation cloud mask for the Multiangle Image SpectroRadiometer (MISR). *J. Atmos. Oceanic Technol.,* **12,** 1215–1228.
Frulla, L. A., J. A. Milovich, and D. A. Gagliardini, 1995: Illumination and observation geometry for NOAA–AVHRR images. *Int. J. Remote Sens.,* **16,** 2233–2253.
Han, Q., W. B. Rossow, and A. A. Lacis, 1994: Near-global survey of effective droplet radii in liquid water clouds using ISCCP data. *J. Climate,* **7,** 465–497.
Hanan, N. P., S. D. Prince, and B. N. Holben, 1995: Atmospheric correction of AVHRR data for biophysical remote sensing of the Sahel. *Remote Sens. Environ.,* **51,** 306–316.
Harshvardhan, and D. A. Randall, 1985: Comments on ''The parameterization of radiation for numerical weather prediction and climate models.'' *Mon. Wea. Rev.,* **113,** 1832–1833.
——, B. A. Wielicki, and K. M. Ginger, 1994: The interpretation of remotely sensed cloud properties from a model parameterization perspective. *J. Climate,* **7,** 1987–1998.
Kneizys, F. X., E. P. Shettle, L. W. Abreu, J. H. Chetwynd Jr., G. P. Anderson, W. O. Gallery, J. E. Selby, and S. A. Clough, 1988: User's guide to LOWTRAN 7. AFGL-TR-88-0177, Air Force Geophysics Laboratory, 137 pp.
Loeb, N. G., 1992: A multispectral retrieval technique for inferring cloud and clear sky properties over the ocean from satellite measurements. M.S. thesis, Dept. of Earth and Atmospheric Science, York University, 186 pp. [Available from National Library of Canada, 395 Wellington Street, Ottawa, ON K1A 0N4, Canada.]
——, and R. Davies, 1996: Observational evidence of plane parallel model biases: The apparent dependence of cloud optical depth on solar zenith angle. *J. Geophys. Res.,* **101,** 1621–1634.
Marshak, A., A. Davis, W. Wiscombe, and G. Titov, 1995a: The verisimilitude of the independent pixel approximation used in cloud remote sensing. *Remote Sens. Environ.,* **52,** 71–78.
——, ——, ——, and R. Cahalan, 1995b: Radiative smoothing in fractal clouds. *J. Geophys. Res.,* **100,** 26 247–26 261.
Masuda, K., 1991: Dependence of shortwave radiation on cirrus cloud parameters and the derivation of cirrus information using satellite observations. Ph.D. thesis, University of Kyoto, 123 pp. [Available from Meteorological Research Institute, 1-1 Nagamine, Tsukuba, Ibaraki 305, Japan.]
Mishchenko, M. I., W. B. Rossow, A. Macke, and A. A. Lacis, 1996: Sensitivity of cirrus cloud albedo, bidirectional reflectance and optical thickness retrieval accuracy to ice particle shape. *J. Geophys. Res.,* **101,** 16 973–16 985.
Oreopoulos, L., 1996: Plane parallel albedo bias from satellite measurements. Ph.D. thesis, McGill University, 142 pp. [Available from National Library of Canada, 395 Wellington Street, Ottawa, ON K1A 0N4, Canada.]
——, and R. Davies, 1998: Plane parallel albedo biases from satellite observations. Part II: Parameterizations for bias removal. *J. Climate,* **11,** 933–944.
Platnick, S., and F. P. J. Valero, 1995: A validation of a satellite cloud retrieval during ASTEX. *J. Atmos. Sci.,* **52,** 2985–3001.
Rossow, W. B., and R. A. Schiffer, 1991: ISCCP cloud data products. *Bull. Amer. Meteor. Soc.,* **72,** 2–20.
Saunders, R. W., and D. P. Edwards, 1989: Atmospheric transmittance for the AVHRR channels. *Appl. Opt.,* **28,** 4154–4160.
Slingo, A., 1989: A GCM parameterization for the shortwave radiative properties of water clouds. *J. Atmos. Sci.,* **46,** 1419–1427.
Stamnes, K., S.-C. Tsay, W. J. Wiscombe, and K. Jayaweera, 1988: Numerically stable algorithm for discrete-ordinates-method radiative transfer in multiple scattering and emitting layered media. *Appl. Opt.,* **27,** 2502–2509.
Stephens, G. L., 1985: Reply. *Mon. Wea. Rev.,* **113,** 1834–1835.
Takano, Y., and K-N. Liou, 1989: Solar radiative transfer in cirrus clouds. Part I: Single-scattering and optical properties of hexagonal ice crystals. *J. Atmos. Sci.,* **46,** 3–19.
Teillet, P. M., and B. N. Holben, 1994: Towards operational radiometric calibration of NOAA AVHRR imagery in the visible and near-infrared channels. *Can. J. Remote Sens.,* **20,** 1–10.
Várnai, T., 1996: Reflection of solar radiation by inhomogeneous clouds. Ph.D. thesis, McGill University, 146 pp. [Available from National Library of Canada, 395 Wellington Street, Ottawa, ON K1A 0N4, Canada.]
Wielicki, B. A., R. D. Cess, M. D. King, D. A. Randall, and E. F. Harrison, 1995: Mission to Planet Earth: Role of clouds and radiation in climate. *Bull. Amer. Meteor. Soc.,* **76,** 2125–2153.